Electronic Supplementary Material (ESI) for Journal of Materials Chemistry A.

Supporting Information

Two-dimensional FeS_2- encapsulated Au: A quasi-epitaxial heterojunction for synergistic catalytic activity under photoelectrocatalytic water reduction

*Indranil Mondal, Song Yi Moon, Hyunhwa Lee, Heeyoung Kim and Jeong Young Park**

Characterization

To investigate the crystalline phase of the different nickel species, multipurpose attachment X-ray diffraction (XRD; SmartLab, RIGAKU) was used. The XRD measurements were taken at a 2θ scan range of 10–90°, scan speed of 2.4°/min, and step size of 0.01 Å using CuK_α radiation to identify the phases. The exterior morphology was inspected using a Magellan 400 scanning electron microscope (SEM). To investigate the morphological characteristics, including the phase, transmission electron microscopy (TEM) was carried out using field emission transmission electron microscopy (FE-TEM; Tecnai TF30 ST). The TEM samples were prepared by drop casting the acetone suspension of each respective catalyst on a 300-mesh copper grid. X-ray photoelectron spectroscopy (XPS) was carried out using a Thermo VG Scientific Sigma Probe system equipped with an Al-Kα X-ray source (1486.3 eV) with an energy resolution of 0.47 eV full width at half maximum under ultrahigh vacuum conditions of 10^{-10} Torr. An ultraviolet–visible–near-infrared (UV–Vis–NIR) spectrometer (Shimadzu, UV3600) was used to characterize the optical properties of the FeS_2-deposited quartz film. Atomic force microscopy (AFM) analysis was performed using an Agilent 5500 model using a Si tip, which worked at a resonant frequency of 331 kHz and 42 N/m force constant.

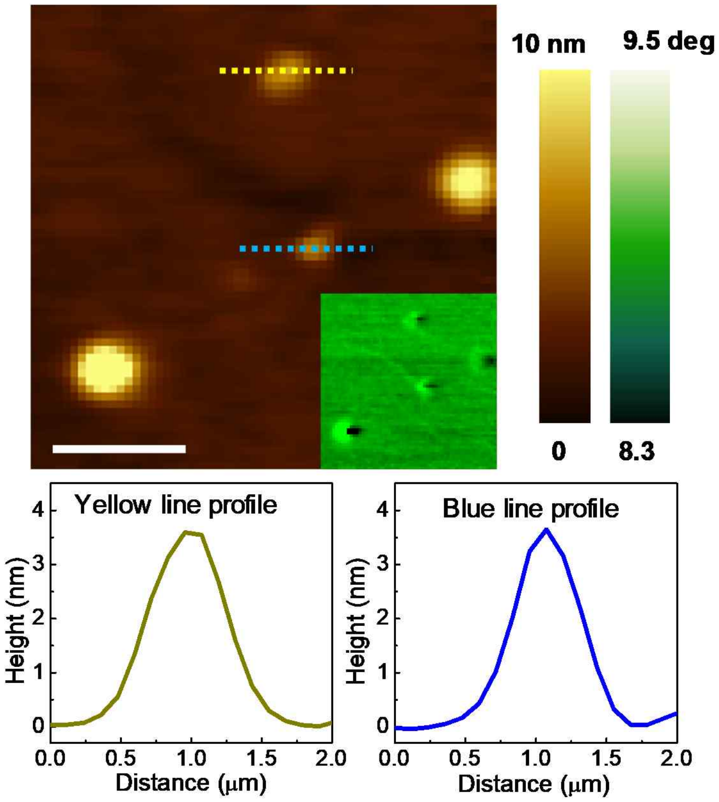

Fig. S1. Non-contact mode AFM topography and height profiles extracted from line scanning at different positions of the sheet-like FeS_2 structure prepared using 2.5 mmol of S^{2-} dispersed on a Si substrate. The inset shows the phase imaging of the FeS_2, which shows the different chemical nature of the FeS_2 compared with that of the Si substrate. From the height profile, the typical height of the FeS_2 nanostructure is 3–4 nm. The scale bar represents 2 μm.

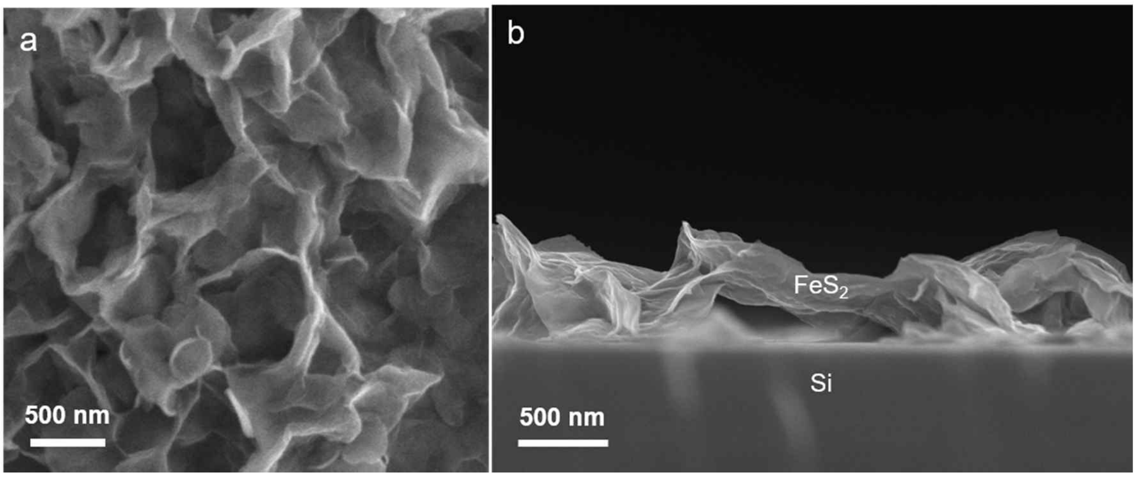

Fig. S2 (a) Top and (b) side views of the FS2.5 nanosheets deposited on *p*-type Si.

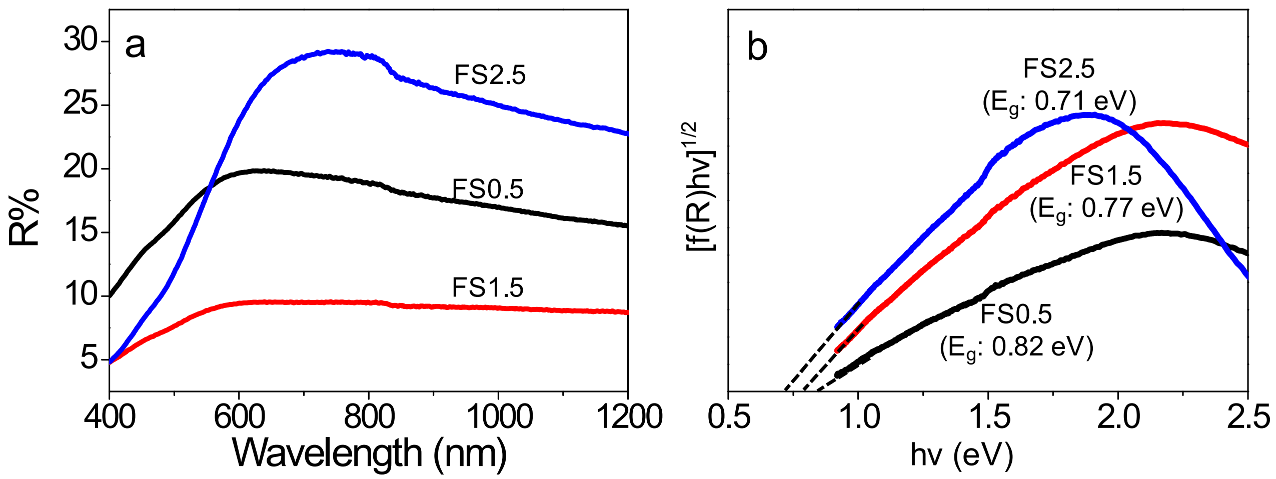

Fig. S3 (a) UV-Vis diffuse reflection spectroscopy of the different FeS_2 catalysts measured with the catalysts deposited on a quartz slide. (b) Estimated band gap of the FeS_2 catalysts using the Tauc plot.

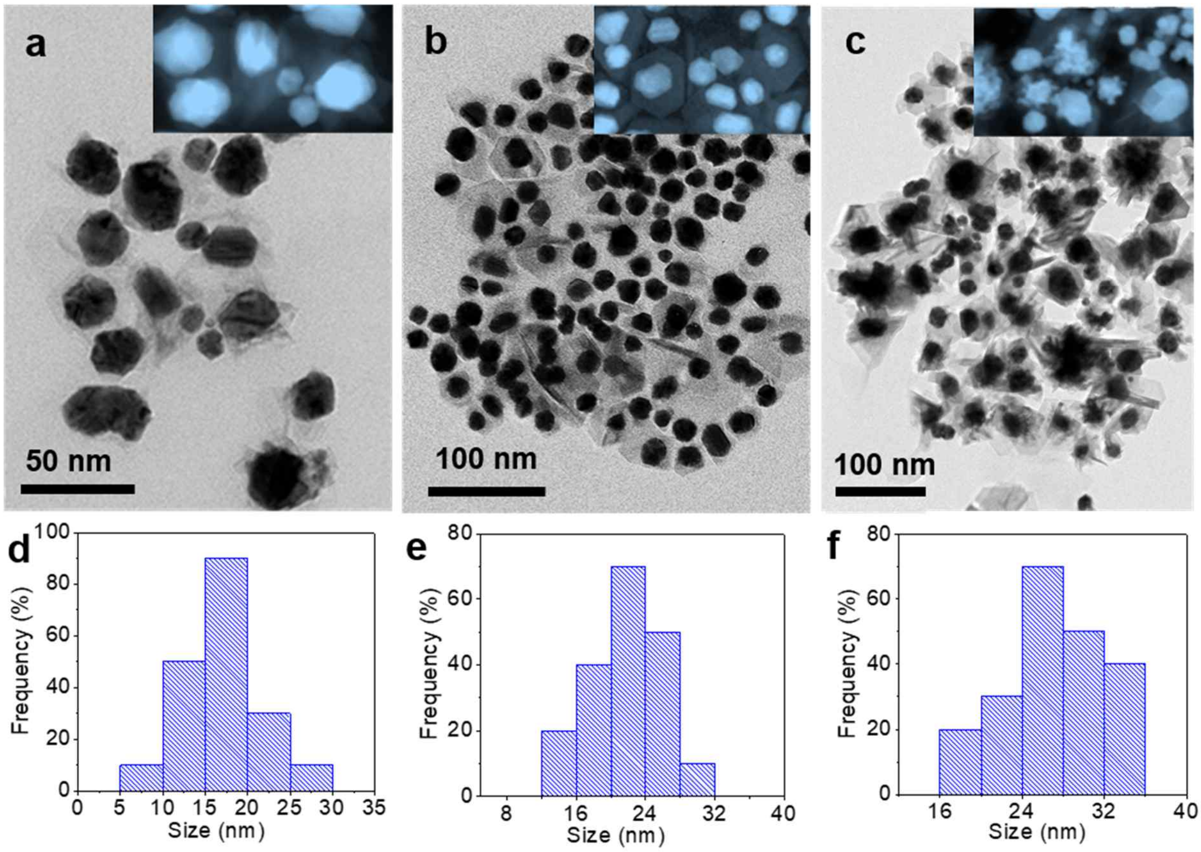

Fig. S4 TEM images of the different Au-FeS$_2$ heterostructures synthesized with (a) 0.5 mmol of S^{2-} (AFS0.5), (b) 1.5 mmol of S^{2-} (AFS1.5), and (c) 2.5 mmol of S^{2-} (AFS2.5). Inset shows the selected area of the HAADF-STEM images with the corresponding nanostructures; size distribution curves of the Au nanoparticles in the Au-FeS$_2$ heterostructures synthesized using (d) 0.5 mmol of S^{2-} (AFS0.5), (e) 1.5 mmol of S^{2-} (AFS1.5), and (f) 2.5 mmol of S^{2-} (AFS2.5).

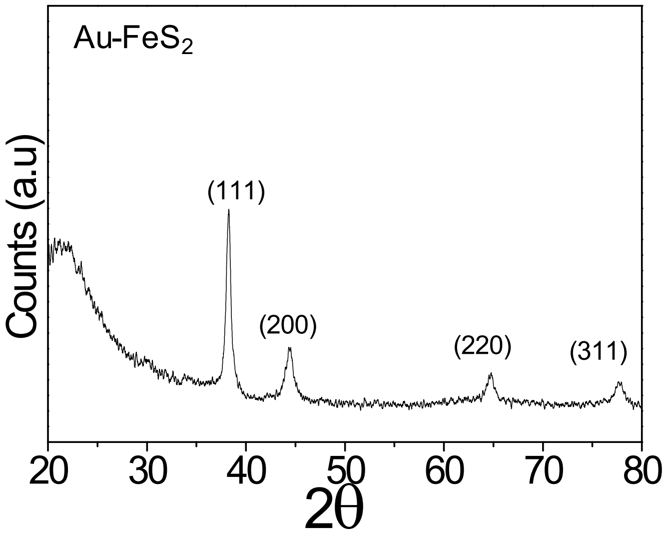

Fig. S5 Powder XRD pattern of the Au-FeS$_2$ heterojunction (AFS1.5).

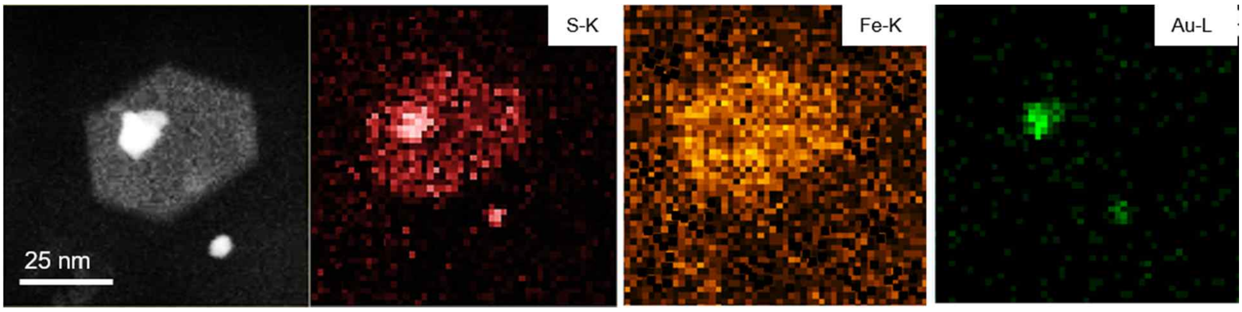

Fig. S6 Elemental mapping images of the Au, Fe, and S in the selected area HADDF-STEM image of AFS1.5.

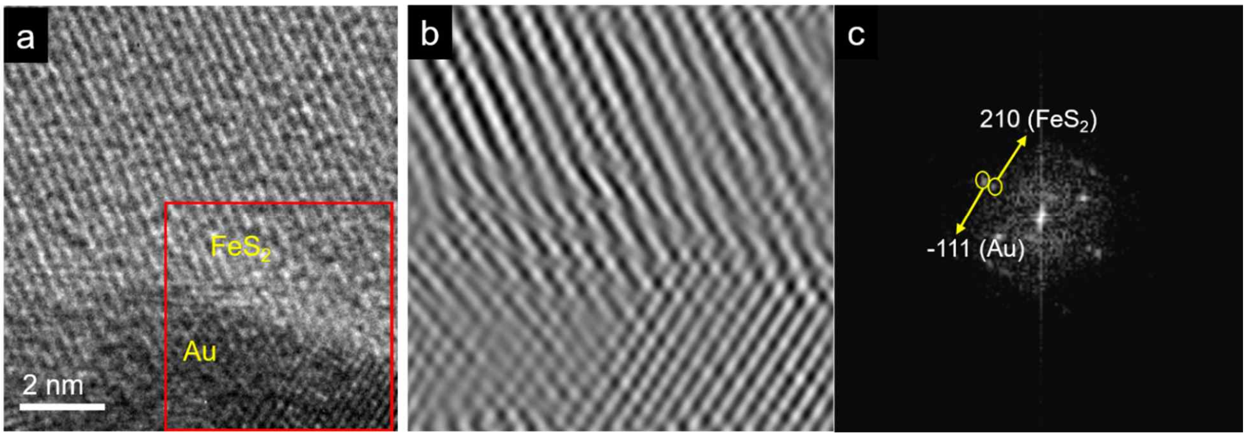

Fig. S7 (a) HRTEM of the Au-FeS$_2$ prepared using 2.5 mmol of S^{2-} (AFS2.5). The TEM was collected where FeS$_2$ is very thin on the Au. (b) Simulated HRTEM obtained from the selected area (red box in (a)) of the HRTEM shows the characteristic plane of pyrite FeS$_2$ and Si. (c) FFT pattern collected from the displayed HRTEM shows the epitaxial relationship between the Au and the FeS$_2$.

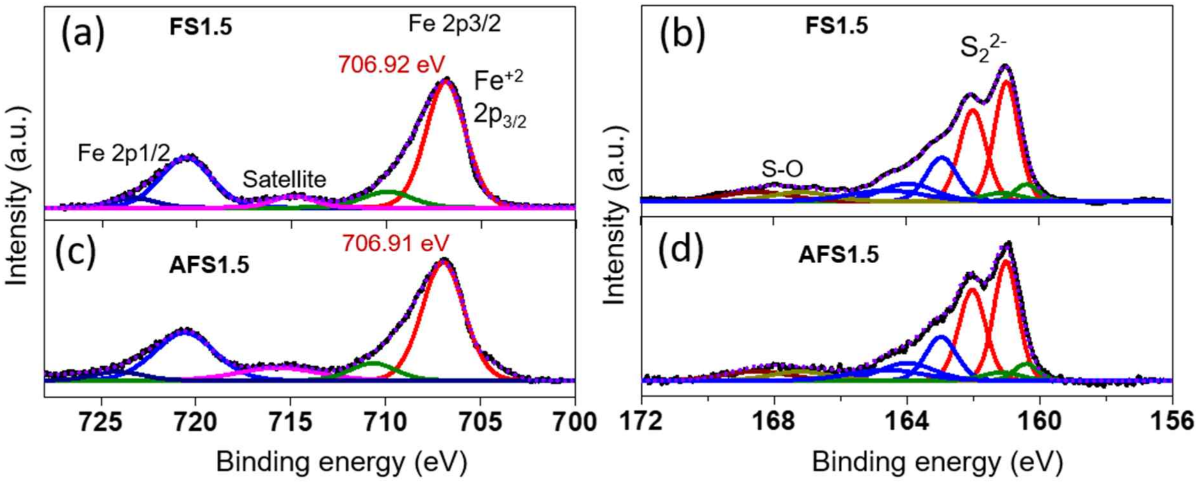

Fig. S8 Fe 2p XPS profiles of (a) FeS_2 (FS1.5) and (c) Au-FeS_2 (AFS1.5) where Fe is predominantly present as Fe^{2+} (red and blue curves) in the pyrite FeS_2, which is coordinated to disulfide. The Fe^{2+} peak in the Fe $2p_{3/2}$ region did not show any shift before or after the heterojunction formation. S 2p XPS profiles of (b) FeS_2 (FS1.5) and (d) Au-FeS_2 (AFS1.5) showing the intrinsic bulk-like (red curves) outer surface (green curves) disulfides with the presence of satellite peaks (blue curves) and surface sulfates (SO_4^{2-}).

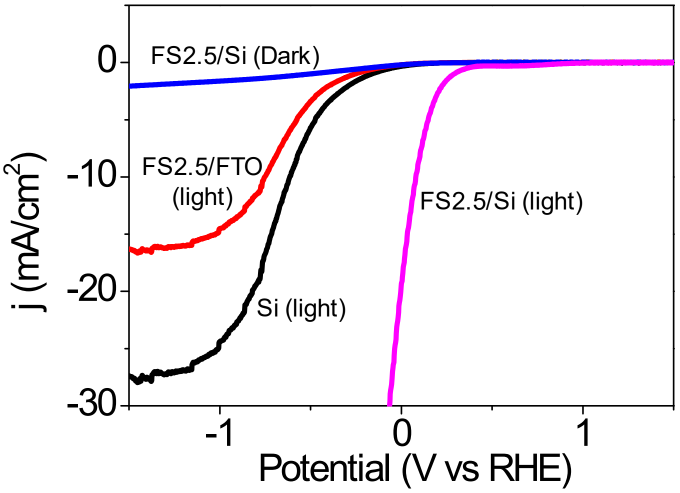

Fig. S9 Typical I–V curves for the different photocathodes at the specified experimental conditions.

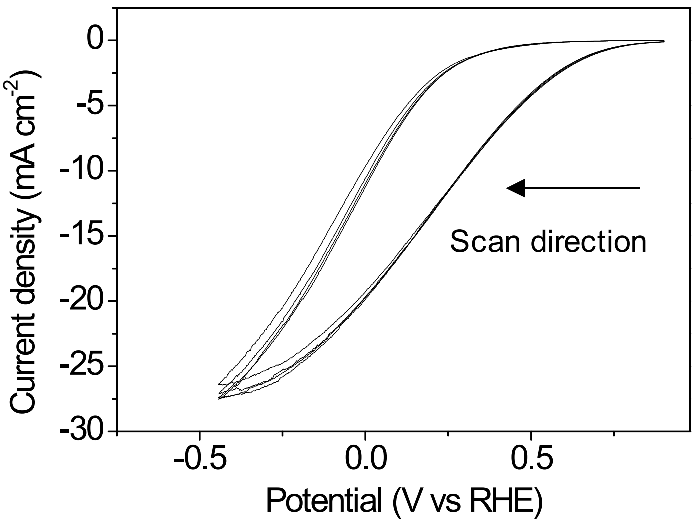

Fig. S10 Four consecutive CV scans of the Au-FeS$_2$(AFS1.5)/Si photoelectrode indicate the reproducibility of the current density value versus potential.

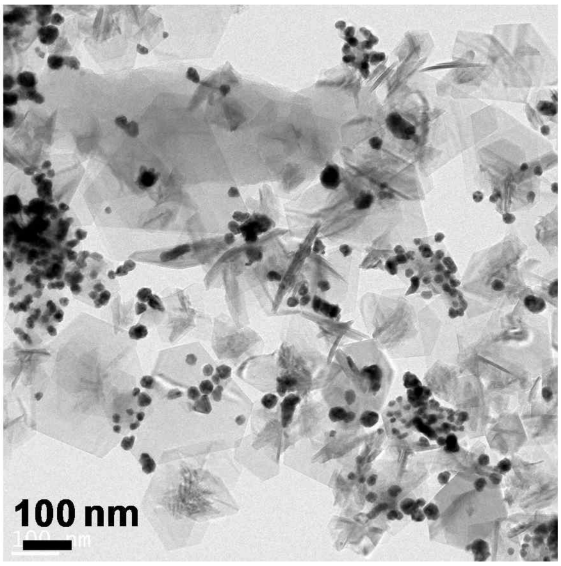

Fig. S11 TEM image of the Au-deposited FeS$_2$. The Au precursor was injected 15 min after the formation of the FeS$_2$. The FeS$_2$ was prepared using the procedure described in the experimental section using a 2.5 mmol concentration of S^{2-}.

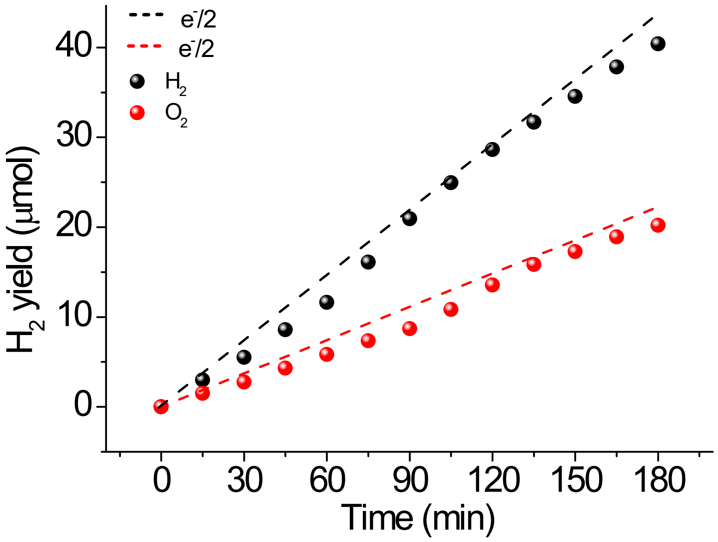

Fig. S12 Temporal plot for the quantitative yield of H_2 and O_2 gases. The calculated faradaic efficiency for the AFS1.5/Si electrode is 95.3%. A slight deviation from 100% faradaic efficiency might be caused by dissolved oxygen participating in the reverse reaction and inevitable gas leaks from the experimental apparatus. The faradaic efficiency was measured using a sealed three-electrode electrochemical reactor in presence of a 0.5 M H_2SO_4 solution. The reactor was first purged and backfilled with ultrapure argon (5 kPa). The evolved gases were analyzed using an online gas chromatography system (DS Science with a thermal conductivity detector, MS-5A column, and argon as the carrier gas) The hydrogen generation yield was measured by auto-sampling every 15 minutes. The faradaic efficiency was determined using the equation

faradaic efficiency (%) = [n_{H2} (experimental)/n_{H2} (theoretical)] x 100.

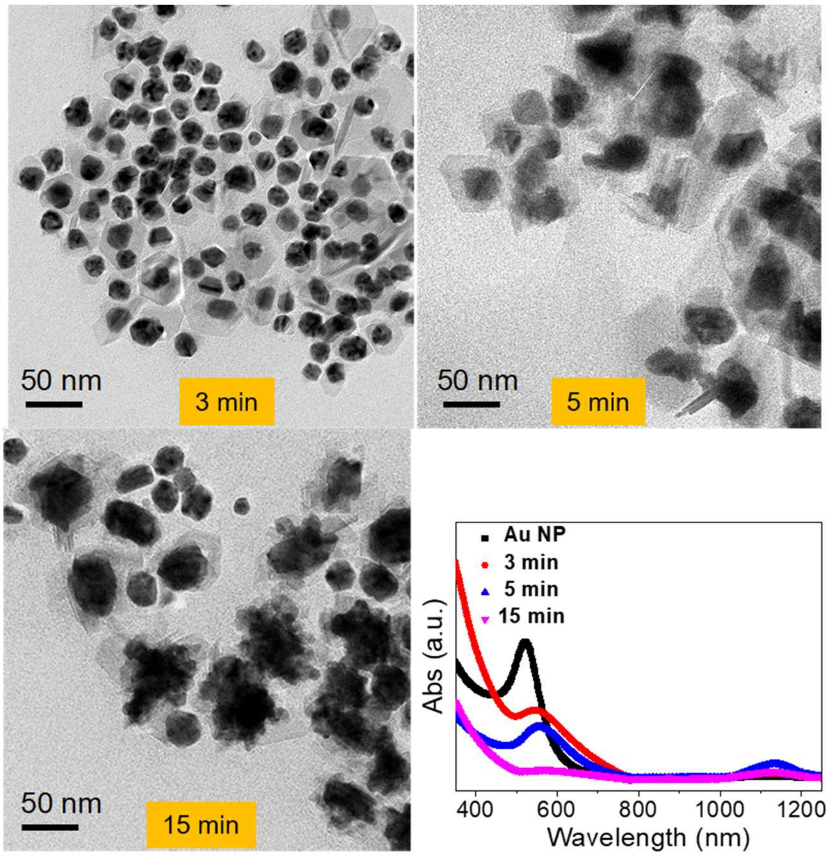

Fig. S13 TEM images of the Au-FeS_2 heterostructures (AFS1.5) collected after different annealing times. The UV-Vis spectra showed a change in the plasmonic properties of the Au after different annealing times.

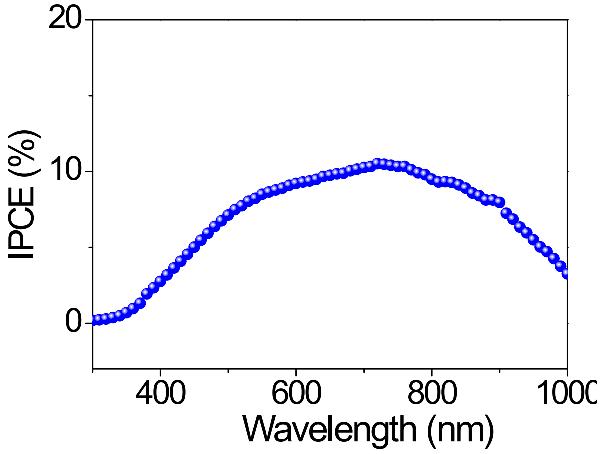

Fig. S14 IPCE plot for the different Si/Au photocathodes measured at the chronoamperometric condition of 0 V.

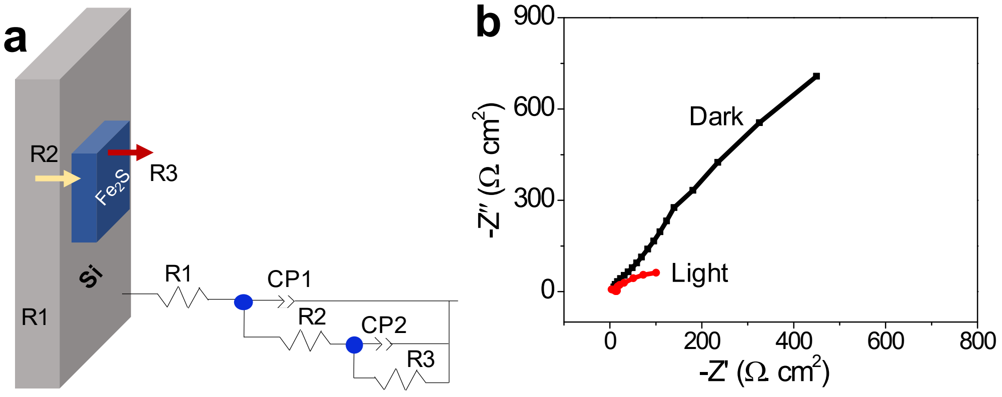

Fig. S15 (a) Equivalent circuit considered for fitting the Nyquist plot. (b) EIS Nyquist plot of the Si/Au-FeS_2 (AFS1.5) photocathode in the dark and with light.

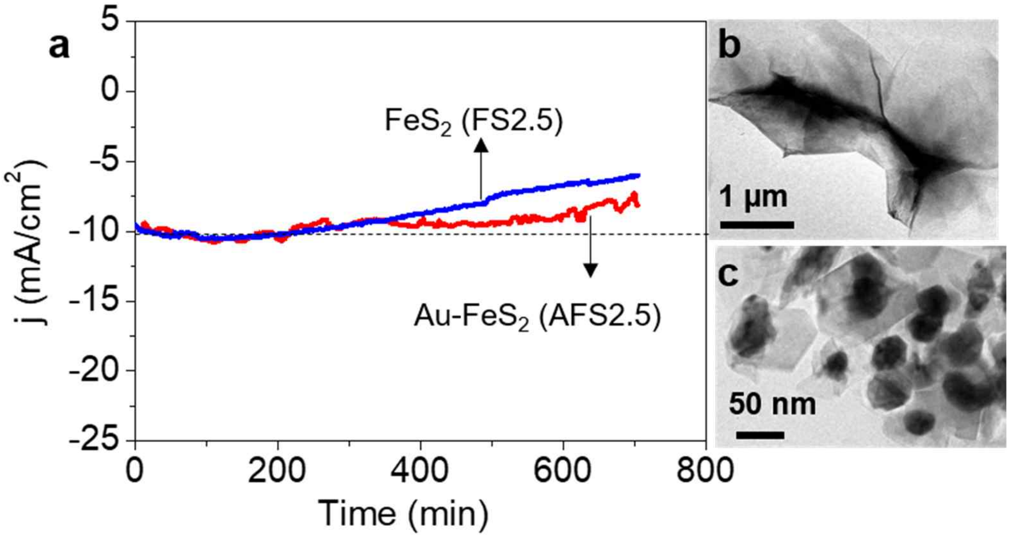

Fig. S16 (a) Stability of the optimized FeS_2 and Au-FeS_2 catalysts measured at 0.08 and 0.22 V, respectively, under illumination. TEM images of the (b) FeS_2 (FS2.5) and (c) Au-FeS_2 (AFS1.5) catalysts collected after the stability test.

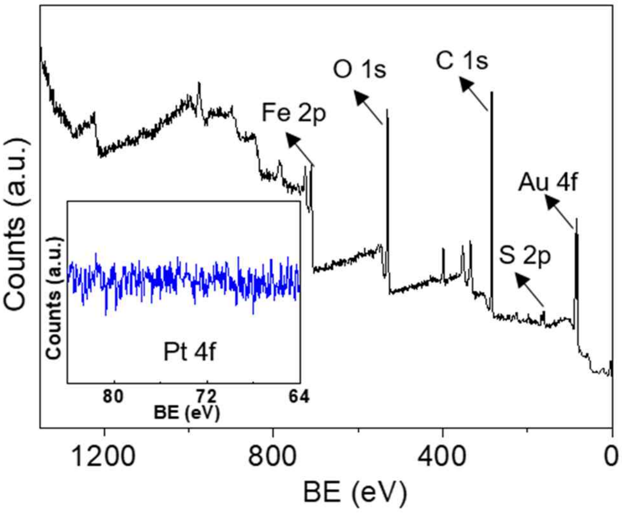

Fig. S17 Full scan survey and Pt 4f XPS profile of the Au-FeS_2 catalyst after the electrochemical reaction. This indicates no Pt contamination of the working electrode during the reaction.

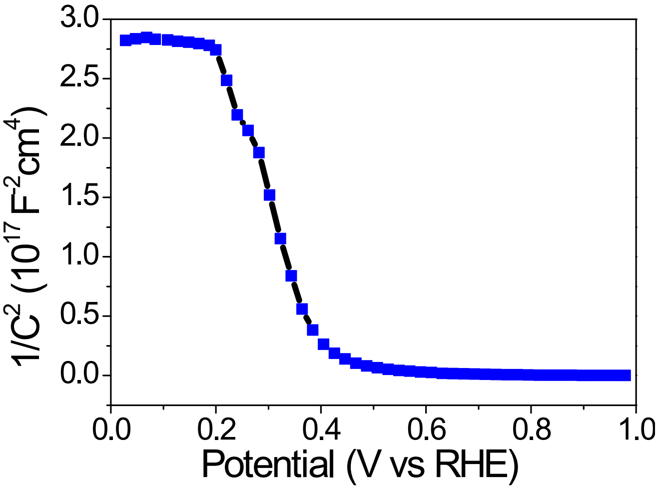

Fig. S18 Mott-Schottky plot of the *p*-type Si recorded under light irradiation.

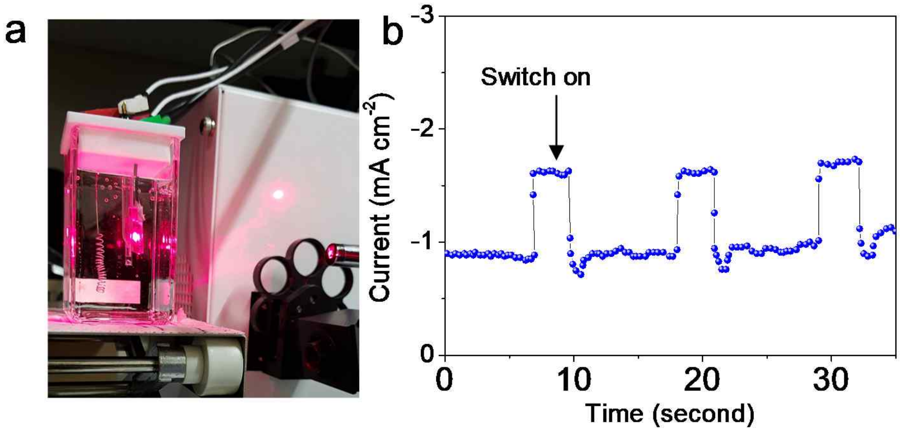

Fig. S19 (a) Image of the 650 nm laser irradiation on the Au-FeS_2/FTO (AFS1.5) photodevice. The illumination intensity was 100 mW cm^{-2}. (b) The chronoamperometric current density value recorded at 0 V potential with chopped illumination.

Table S1 Comparison of the activities for the different Si-based photocathodes. Each experiment was carried out at the same light intensity of 100 mW cm^{-2}.

Photocathode	**Cathodic photocurrent**	**Applied potential (V) vs RHE**	**Electrolyte**	**Reference**
Au nanorod on MoS_2 sheet	10 mA cm^{-2}	−0.26	0.1 M KCl	1
MoS_x/n$^+$P Si	10 mA cm^{-2}	−0.4	1.0 M $HClO_4$	*2*
Graphite/exfoliated graphene/Co_9S_8/Ni_3Se_2 in two electrode cell system	40 mA cm^{-2}	−0.3	1.0 M KOH	3
Metallic 1T-MoS_2 and planar p-type Si	17.5 mA cm^{-2}	0.0	0.5 M H_2SO_4	4
Ni_3S_4 surface modified with S^{2-} and Ni^{2+}	5 mA cm^{-2}	0.0	0.5 M Na_2SO_4, 0.25 M Na_2HPO_4, and 0.25 M NaH_2PO_4	5
Plasmonic Cu_2S with defects (without any semiconductor)	0.6 mA cm^{-2}	0.0	1.0 M KCl	6
a-$CoMoS_x$ on Si	17.5 mA cm^{-2}	0.0	Acidic phosphate buffered to pH 4.5	7
WS_2 on Si nanowire	18.8 mA cm^{-2}	0.0	0.05 M H_2SO_4	8
Cu_2O/g-C_3N_4/WS_2 triple-layer photocathode (in visible light)	9.5 mA cm^{-2}	−0.55	1.0 M Na_2SO_4	9

Cobalt sulfide nanoparticle implanted porous organic polymer	6.43 mA cm^{-2}	0	0.5 M Na_2SO_4	10
Cu_2S thin layers on Cu_2O nanowires	5.05 mA cm^{-2}	0	1 M Na_2SO_4 (supporting electrolyte + 0.1 M KH_2PO_4); pH 4.5	11
Ultrathin Pt layer on Au-nanoisland modified Si photocathode	10 mA cm^{-2}	−1.0	0.1 M H2SO4 electrolyte	12
Photoassisted electrochemically Pt deposited p-Si	10 mA cm^{-2}	−0.18	1 M H_2SO_4	13
Pt /Ti/SiO_2/Si	10 mA cm^{-2}	−0.12	0.5 M H_2SO_4	14
Si microwire with doped heterometal MoS_2	10 mA cm^{-2}	0.07	0.5 M H_2SO_4	15
Au-FeS_2 co-axial heterostructure	10 mA cm^{-2}	0.22	0.2 M H_2SO_4	This work

Table S2 Charge transfer resistance values evaluated from the electrochemical impedance spectra that were fitted on equivalent circuits having different constant phase elements.

Catalyst	**$R_{ct,Si}$ (Ω cm^2)**	**$R_{ct,cat}$ (Ω cm^2)**
FS0.5	27.11	1171
FS1.5	24.54	1108.7
FS2.5	15.8	932.5
AFS0.5	13.72	769.8
AFS1.5	12.4	418.3
AFS2.5	10.6	506.8

Table S3 Photoluminescence decay parameters and average lifetimes for the different FeS_2 catalysts.

Catalyst	τ_1	τ_2	a_1	a_2	τ_{av}
FS0.5	0.2677 ns	0.8253 ns	10787.228	506.124	0.292 ns
FS1.5	0.2980 ns	0.9125 ns	10639.514	488.945	0.325 ns
FS2.5	0.3976 ns	0.8941 ns	11253.061	332.194	0.412 ns

References

1. Y. Shi, J. Wang, C. Wang, T. T. Zhai, W. J. Bao, J. J. Xu, X. H. Xia, H. Y. Chen, *J. Am. Chem. Soc.*, 2015, **137**, 7365−7370.
2. B. Seger, A. B. Laursen, P. C. Vesborg, T. Pedersen, O. Hansen, S. Dahl, I. Chorkendorff, *Angew. Chem., Int. Ed.,* 2012, **51**, 9128−9131.
3. Y. Hou, M. Qiu, G. Nam, M. G. Kim, T. Zhang, K. Liu, X. Zhuang, J. Cho, C. Yuan, X. Feng, *Nano Lett.,* 2017, **17**, 4202−4209.
4. Q. Ding, F. Meng, C. R. English, M. Cabán-Acevedo, M. J. Shearer, D. Liang, A. S. Daniel, R. J. Hamers, S. Jin, *J. Am. Chem. Soc*., 2014, **136**, 8504−8507.
5. S. Kim, T. Nishino, M. Saruyama, M. Sakamoto, H. Kobayashi, S. Akiyama, T. Yamada, K. Domen, T. Teranishi, *ChemNanoMat,* 2017, **3** 764–771.
6. K. Ren, P, Yin, Y. Zhou, X. Cao, C. Dong, L. Cui, H. Liu, X. Du, *Small,* 2017, 13(1700867*)*.
7. Y. Chen, P. D. Tran, P. Boix, Y. Ren, S. Y. Chiam, Z. Li, K. Fu, L. H. Wong, J. Barber, *ACS Nano,* 2015, **9**, 3829−3836.
8. Z. Huang, C. Wang, Z. Chen, H. Meng, C. Lv, Z. Chen, R. Han, C. Zhang, *ACS Appl. Mater. Interfaces,* 2014, **6**, 10408−10414.
9. X. Xu, Y. Liu, Y. Zhu, X. Fan, Y. Li, F. Zhang, G. Zhang, W. Peng, *ChemElectroChem,* 2017, **4**, 1498–1502.
10. S. C. Shit, S. Khilari, I. Mondal, D. Pradhan, J. Mondal, *Chem. Eur. J.,* 2017, **23**, 14827–14838.
11. Z. Li, Z. Zhang, *Nano Res*., 2018, **11**, 1530–1540.
12. C. Das, M. Kot, Z. Rouissi, K. Kędzierski, K. Henkel, D. Schmeißer, *ACS Omega,* 2017, **2**, 1360−1366.
13. C. U. Maier, M. Specht, G. Bilger, *Int. J. Hydrogen Energy*, 1996, **21**, 859–864.
14. D. V Esposito, I. Levin, T. P. Moffat, A. A. Talin, *Nat. Mater*., 2013, **12**, 562–568.
15. C-J Chen, K-C. Yang, C-W. Liu, Y-R. Lud, C-L. Dong, D-H. Wei, S-F. Hu, R-S. Liu, *Nano Energy,* 2017, **32**, 422–432.